

**COSMOS-3D: Two obscured X-ray AGNs with hot dust and He I $\lambda$ 10830 absorption at  $z \sim 3$** 

ZI-JIAN LI ,<sup>1,2</sup> SIWEI ZOU ,<sup>1,3</sup> JIANWEI LYU ,<sup>4</sup> JACLYN B. CHAMPAGNE ,<sup>4</sup> JIA-SHENG HUANG ,<sup>1,5</sup> CHENG CHENG ,<sup>1</sup> SHUQI FU ,<sup>6,7</sup> ZIJIAN ZHANG ,<sup>6,7</sup> DANYANG JIANG ,<sup>6,7</sup> KHEE-GAN LEE ,<sup>8,9</sup> FEIGE WANG ,<sup>10</sup> XIAOHUI FAN ,<sup>4</sup> JINYI YANG ,<sup>10</sup> RUANCUN LI ,<sup>6,7</sup> HOLLIS B. AKINS ,<sup>11,12</sup> FUYAN BIAN ,<sup>13</sup> ANDREAS L. FAISST ,<sup>14</sup> LUIS C. HO ,<sup>6,7</sup> KOHEI INAYOSHI ,<sup>6</sup> LINHUA JIANG ,<sup>6,7</sup> XIANGYU JIN ,<sup>10</sup> KOKI KAKIUCHI ,<sup>15,16</sup> JEYHAN S. KARTALTEPE ,<sup>17</sup> ZIHAO LI ,<sup>15,16</sup> WEIZHE LIU ,<sup>4</sup> JAN-TORGE SCHINDLER ,<sup>18</sup> AND WEI LEONG TEE ,<sup>19</sup>

<sup>1</sup>Chinese Academy of Sciences South America Center for Astronomy, National Astronomical Observatories, CAS, Beijing 100101, China

<sup>2</sup>School of Astronomy and Space Sciences, University of Chinese Academy of Sciences, Beijing 100049, China

<sup>3</sup>Departamento de Astronomía, Universidad de Chile, Casilla 36-D, Santiago, Chile

<sup>4</sup>Steward Observatory, University of Arizona, 933 N Cherry Ave, Tucson, AZ, 85721, USA

<sup>5</sup>Harvard-Smithsonian Center for Astrophysics, 60 Garden Street, Cambridge, MA 02138, USA

<sup>6</sup>Kavli Institute for Astronomy and Astrophysics, Peking University, Beijing 100871, China

<sup>7</sup>Department of Astronomy, School of Physics, Peking University, Beijing 100871, People's Republic of China

<sup>8</sup>Kavli IPMU (WPI), UTIAS, The University of Tokyo, Kashiwa, Chiba 277-8583, Japan

<sup>9</sup>Center for Data-Driven Discovery, Kavli IPMU (WPI), UTIAS, The University of Tokyo, Kashiwa, Chiba 277-8583, Japan

<sup>10</sup>Department of Astronomy, University of Michigan, 1085 S. University Ave., Ann Arbor, MI 48109, USA

<sup>11</sup>Department of Astronomy, The University of Texas at Austin, 2515 Speedway Boulevard Stop C1400, Austin, TX 78712, USA

<sup>12</sup>Cosmic Frontier Center, The University of Texas at Austin, Austin, TX 78712, USA

<sup>13</sup>European Southern Observatory, Alonso de Cordova 3107, Casilla 19001, Vitacura, Santiago 19, Chile

<sup>14</sup>IPAC, California Institute of Technology, 1200 E. California Blvd. Pasadena, CA 91125, USA

<sup>15</sup>Cosmic Dawn Center (DAWN), Denmark

<sup>16</sup>Niels Bohr Institute, University of Copenhagen, Jagtvej 128, DK-2200, Copenhagen N, Denmark

<sup>17</sup>Laboratory for Multiwavelength Astrophysics, School of Physics and Astronomy, Rochester Institute of Technology, 84 Lomb Memorial Drive, Rochester, NY 14623, USA

<sup>18</sup>Hamburger Sternwarte, University of Hamburg, Gojenbergsweg 112, D-21029 Hamburg, Germany

<sup>19</sup>Department of Astronomy and Astrophysics, The Pennsylvania State University, 525 Davey Lab, University Park, PA 16802, USA

## ABSTRACT

We report the discovery of two broad-line X-ray AGNs (`cid_414` and `cid_947`) at  $z \sim 3$  that exhibit prominent He I $\lambda$ 10830 + Pa $\gamma$  emission and absorption, identified from the JWST Cycle 3 large GO treasury program COSMOS-3D using NIRCam F444W grism spectroscopy. Additional UV/optical line measurements (e.g., Ly $\alpha$ , Si IV, C IV) come from complementary COSMOS-field spectroscopy. Both sources are robustly detected in the mid-infrared, with detections in MIRI F1000W for both AGNs and an additional detection in MIRI F2100W for `cid_414`, indicating the presence of hot dust emission. The source `cid_947` shows a higher He I $\lambda$ 10830 absorption column density and X-ray-inferred  $N_{\text{H}}$ , and displays strong outflow signatures in He I, Si IV, and C IV with velocity offsets exceeding 5000 km s $^{-1}$ . The source `cid_414` shows a narrow Ly $\alpha$  emission line with luminosity  $\log L_{\text{Ly}\alpha} = 42.49 \pm 0.01$  erg s $^{-1}$  and a higher intrinsic 2–10 keV X-ray luminosity. Host-galaxy decomposition and multi-component SED fitting indicate that `cid_947` hosts a more massive black hole but lower star formation rate than `cid_414`. From simplified photoionization modeling, we infer that the dense absorbing gas has a characteristic size comparable to the nuclear broad-line region and is likely kinematically coupled to the obscuration associated with the dust torus. He I $\lambda$ 10830 absorption has also been identified in several compact little red dots at similar redshifts. Together with the two AGNs reported here, these findings suggest that dense circumnuclear gas are plausibly prevalent at high redshift and plays an important role in regulating AGN obscuration and black hole–host co-evolution.

*Keywords:* Active galactic nuclei (16) — AGN host galaxies (2017) — Dust shells (414)

## 1. INTRODUCTION

The growth of supermassive black holes and the evolution of their host galaxies are closely connected through

the presence and dynamics of dense gas in the circumnu-

clear region. Obscuration represents a key phase in this co-evolution, where gas and dust surrounding the active nucleus attenuate the emergent radiation and generate characteristic absorption and emission signatures in the spectrum (see the review of [R. C. Hickox & D. M. Alexander 2018](#) and references therein). However, the physical processes that govern the structure and evolution of the obscuring gas, and how this gas regulates both black hole accretion and star formation in the host galaxy, remain poorly understood.

Theoretical modeling suggests that the hydrogen volume density in the circumnuclear region can exceed  $n_{\text{H}} \gtrsim 10^8 \text{ cm}^{-3}$  ([J. Baldwin et al. 1995](#); [Q. Wu et al. 2025](#)). Observationally, a large fraction of local AGNs are obscured ([E. Treister & C. M. Urry 2006](#); [Z.-J. Li et al. 2024](#)). Hard X-ray measurements from the Swift–BAT all-sky survey (BASS) show that about 70% of nearby AGNs are obscured ([M. Koss et al. 2017](#); [C. Ricci et al. 2017a](#)), while the obscured fraction at higher redshift remains uncertain ([J. Lyu et al. 2024](#)).

$\text{He I}\lambda 10830$  absorption offers distinct advantages for probing the physical conditions of the circumnuclear absorbing gas. The  $\text{He I}\lambda 10830$  transition arises from recombination of  $\text{He}^+$  to the metastable  $2^3\text{S}$  level (ionization potential of 24.56 eV). Because the diffuse stellar radiation field is weak above 24.56 eV ([T. Ji et al. 2015](#)), the presence of  $\text{He I}\lambda 10830$  absorption is a robust indicator of AGN ionization. Moreover, its large oscillator strength ( $f = 0.5392$ ) provides a wider dynamic range in column density compared to commonly used UV resonant lines such as  $\text{C IV}$  and  $\text{Si IV}$  ([K. M. Leighly et al. 2014](#)). However, because  $\text{He I}\lambda 10830$  lies outside the typical optical spectral window, reported detections remain limited. [W.-J. Liu et al. \(2015\)](#) compiled only 11 quasars with  $\text{He I}\lambda 10830$  absorption known at the time, most at  $z < 1$ . The first data release of NIR spectroscopy from the BASS survey identified 7 out of 102 local X-ray AGNs with possible  $\text{He I}\lambda 10830$  absorption, and the number continues to grow in later releases (see, e.g., Figure 2 in [F. Ricci et al. 2022](#)).

The advent of JWST has enabled higher sensitivity and broader wavelength coverage in the near- and mid-infrared. One of the most intriguing discoveries from JWST is a population of compact, red sources known as “little red dots” (LRDs), which exhibit a characteristic V-shaped spectral energy distribution, with rest-frame UV continua that are bluer than the optical ones and a turnover near the Balmer break. Their physical nature is still under debate, with the main discussion focusing on the relative contribution from host galaxies versus AGN emission. Several studies interpret LRDs as dust-reddened AGNs at early cosmic times (e.g., [Y.](#)

[Harikane et al. 2023](#); [D. D. Kocevski et al. 2023](#); [R. Maiolino et al. 2024](#); [J. Matthee et al. 2024](#)). Models in [K. Inayoshi & R. Maiolino \(2025\)](#) suggest that very dense gas with  $n_{\text{H}} > 10^9 \text{ cm}^{-3}$  surrounding the nucleus can reproduce the observed SED shape. Balmer absorption has been reported in LRDs at  $z \sim 4\text{--}6$  (e.g., [X. Lin et al. 2024](#)), where at least 20% of high-redshift AGNs in the broad  $\text{H}\alpha$ -faint sample show absorption features. A small number of LRDs also show  $\text{He I}\lambda 10830$  absorption ([I. Juodžbalis et al. 2024](#); [B. Wang et al. 2025b](#); [R. P. Naidu et al. 2024](#); [V. Kokorev et al. 2025](#)). [I. Juodžbalis et al. \(2024\)](#) proposed that the outflow traced by  $\text{He I}\lambda 10830$  absorption may originate between the broad-line region and the dusty torus in X-ray weak AGNs. JWST/NIRSpec has confirmed  $\text{He I}\lambda 10830$  absorption in X-ray AGNs at  $z \sim 2.5$  ([F. Loiacono et al. 2025](#)), and these objects may be associated with large-scale overdensities ([R. P. Naidu et al. 2024](#)). [B. Wang et al. \(2025b\)](#) found that the kinetic power of the  $\text{He I}\lambda 10830$  outflow is less than one percent of the AGN bolometric luminosity, implying that the outflow itself is unlikely to drive strong AGN feedback. Interestingly, [X. Lin et al. \(2025\)](#) identified three local analogs of LRDs in SDSS, all of which also show  $\text{He I}\lambda 10830$  absorption.

In this letter, we report the detections of two AGNs at  $z \sim 3$  in the COSMOS field with both X-ray and MIRI observations. Both sources exhibit broad  $\text{He I}\lambda 10830$  emission (full width at half maximum,  $\text{FWHM} > 2000 \text{ km s}^{-1}$ ) and prominent absorption features, indicating the presence of dense gas surrounding the broad-line region. The  $\text{He I}\lambda 10830$  spectra and MIRI data are drawn from the JWST GO 3 large program COSMOS-3D (hereafter C3D, PID #5893; PI: K. Kakiichi), which provides F444W NIRCam grism spectroscopy along with MIRI F1000W and F2100W imaging. The data come from observations conducted between December 2024 and May 2025. An overview of the program and its major science goals will be presented in Kakiichi et al., in prep. In Section 2, we describe the target selection and ancillary datasets. Section 3 presents measurements of the AGN properties, including stellar mass ( $M_*$ ), black hole mass ( $M_{\text{BH}}$ ), and star formation rate (SFR). In Section 4, we discuss the role of dense gas traced by  $\text{He I}\lambda 10830$  absorption in obscuration and black hole growth. Section 4.1 models the photoionization state of this gas, and Section 4.3 compares these two AGNs with other populations, including LRDs.

Throughout the paper, we adopt a standard  $\Lambda\text{CDM}$  cosmology with  $H_0 = 70 \text{ km s}^{-1} \text{ Mpc}^{-1}$ ,  $\Omega_M = 0.3$  and  $\Omega_\lambda = 0.7$ . The initial mass function (IMF) adopted in this paper is from [G. Chabrier \(2003\)](#).

## 2. TARGET SELECTION AND OBSERVATIONS

### 2.1. *Target selection*

The two AGNs were first selected from the X-ray catalog of the Chandra COSMOS-Legacy (CCL) Survey (F. Civano et al. 2016), which is a 4.6 Ms *Chandra* program covering 2.2 deg<sup>2</sup> of the COSMOS field. S. Marchesi et al. (2016) reported X-ray properties for 1,855 sources with  $>30$  net counts and derived intrinsic hydrogen absorption column density ( $N_{\text{H}}$ ) and rest-frame 2 to 10 keV luminosities ( $L_{\text{X},2-10\text{keV}}$ ). Among the 1,238 X-ray AGNs ( $\log L_{\text{X},2-10\text{keV}} > 42$ , AGN selection criteria from D. M. Alexander et al. 2005) with secure spectroscopic redshifts, 342 fall within the C3D NIRCam imaging footprint, and 106 of these 342 are covered by C3D MIRI observations (either 1000W or 2100W). We visually inspected the F444W grism spectra of these 106 AGNs, and two of them, `cid_414` and `cid_947`, show prominent He I  $\lambda 10830$  absorption features. The information and measured properties of these two AGNs described in Section 3 are listed in Table 1. We refer to Fu et al. (submitted), who report `cid_414` and another X-ray AGN as two LRDs transitioning into quasars at  $z \sim 3$ , providing detailed rest-frame UV data and discussion. In this work, we focus on investigating the roles of absorbing gas and hot dust at different stages of black hole growth.

### 2.2. *JWST NIRCam and MIRI imaging*

These two targets are covered by both C3D and the GO1 treasury program COSMOS-Web (PI: C. Casey, PID #1727). In C3D, we conducted NIRCam grism spectroscopy using F444W filter, with the F200W filter simultaneously employed in the short-wavelength (SW) channel during the WFSS observations. Direct imaging was obtained with the F115W and F356W filters, providing a total NIRCam coverage of  $\sim 1151$  arcmin<sup>2</sup>. COSMOS-Web have NIRCam imaging in four filters (F115W, F150W, F277W, F444W) and MIRI F770W in parallel. We obtained the COSMOS-Web data from their DR1 data and catalog release 1 (M. Shuntov et al. 2025)<sup>20</sup>. All images (both NIRCam and MIRI) are drizzled to a 0.03" pixel scale. For C3D, we performed the NIRCam and MIRI imaging reduction on F115W, F200W and F356W bands using the JWST pipeline version 1.16.1 (H. Bushouse et al. 2025), with the CRDS calibration reference file context `jwst.1303.pmap`.

The C3D MIRI data (F1000W and F2100W) were processed following the approach adopted in the Systematic Mid-infrared Instrument Legacy Extragalactic Survey

(SMILES; J. Lyu et al. 2024). During Stage 2 reduction, we implemented a customized external background subtraction module from the Rainbow Database JWST pipeline, which constructs a super-background model to suppress cosmic-ray-induced artifacts (J. Álvarez-Márquez et al. 2023).

### 2.3. *JWST Grism spectra*

The WFSS spectra were taken in the F444W filter with Grism R. The  $5\sigma$  line flux limit is  $4 \times 10^{-18}$  erg s<sup>-1</sup> cm<sup>-2</sup> at  $\sim 4.5$   $\mu\text{m}$  (i.e.,  $m_{\text{F444W}} \lesssim 27.5$ ) within the C3D NIRCam coverage. The spectral resolution is  $R \sim 1600$  at  $\sim 4 \mu\text{m}$ . We reduced the grism data following the method described in F. Sun et al. (2023)<sup>21</sup>. We briefly describe the procedure as follows: the Stage 1 data were processed with the standard JWST pipeline. The data were flat fielded using imaging flats taken with the same filter and module, and the sky background was removed using sigma-clipped median grism frames. The wavelength and spectral tracing solutions were derived from commissioning calibrations and refined using field dependent grism trace and dispersion models. Flux calibration was performed using spectra of the standard star P330-E, and the calibrated 2D spectra were extracted and combined for all F444W grism exposures.

### 2.4. *Ancillary data*

The COSMOS field provides extensive multiwavelength ancillary observations, allowing a detailed characterization of these two targets from X-ray to radio. Below we summarize the datasets used in this work.

#### 2.4.1. *X-ray*

We use the reduced archival X-ray data from the CCL survey and its X-ray catalog (S. Marchesi et al. 2016) in this work (see Figure A1). CCL survey has a hard-band 2-10 keV flux limit of  $1.5 \times 10^{-15}$  erg s<sup>-1</sup> cm<sup>-2</sup>. The data were reduced with CIAO 4.5 (A. Fruscione et al. 2006) and CALDB 4.5.9. The intrinsic 2-10 keV X-ray luminosity  $L_{2-10,\text{keV}}$  and the absorbing column density  $N_{\text{H}}$  are derived from spectral fits using an absorbed power-law model and the photon index  $\Gamma$  is fixed at 1.9 in the fitting. Details of the X-ray spectral fitting are provided in S. Marchesi et al. (2016). The  $L_{2-10 \text{ keV}}$  of `cid_414` is  $L_{2-10 \text{ keV}} = 10^{45.17}$  erg s<sup>-1</sup> with a hydrogen column density  $N_{\text{H}} = 10^{22.5}$  cm<sup>-2</sup>. For `cid_947`, the  $L_{2-10 \text{ keV}}$  is  $10^{44.62}$  erg s<sup>-1</sup> and the column density is  $N_{\text{H}} = 10^{23.47}$  cm<sup>-2</sup>. Both sources are therefore classified as Compton-thin ( $N_{\text{H}} < 10^{24}$  cm<sup>-2</sup>) obscured AGN

<sup>20</sup> <https://cosmos2025.iap.fr/>

<sup>21</sup> [https://github.com/fengwusun/nircam\\_grism](https://github.com/fengwusun/nircam_grism)

**Table 1.** Physical properties of the two AGNs. Stellar mass, black hole mass, and SFR are derived from **CIGALE** SED fitting, except for the stellar mass of **cid\_414**, which is estimated from the mass to light ratio. Details are provided in Section 3.4.

cid_414	
RA, DEC	149.89197, 2.28509
Redshift	2.933
$\log L_{X,2-10 \text{ keV}}$ (erg s $^{-1}$ )	45.17
$\log L_{\text{bol}}$ (erg s $^{-1}$ )	46.69
$\log N_{\text{H}}$ (cm $^{-2}$ )	$22.50^{+0.33}_{-1.16}$
$\log M_{*}/M_{\odot}$	$10.92^{+0.29}_{-0.29}$
$\log \text{SFR}$ (M $_{\odot}$ yr $^{-1}$ )	$2.55^{+0.19}_{-0.19}$
$\log M_{\text{BH}}/M_{\odot}$	$9.15^{+0.4}_{-0.4}$
$\lambda_{\text{Edd}}$	$0.28^{+0.41}_{-0.18}$
$f_{\text{HeI}\lambda 10830}$ emission (10 $^{-17}$ erg s $^{-1}$ cm $^{-2}$ )	$5.94^{+0.15}_{-0.15}$
FWHM $_{\text{HeI}\lambda 10830}$ broad (km s $^{-1}$ )	$3591.15^{+77.87}_{-77.87}$
FWHM $_{\text{HeI}\lambda 10830}$ narrow (km s $^{-1}$ )	$1192.77^{+32.18}_{-32.18}$
EW $_{\text{HeI}\lambda 10830}$ emission broad (Å)	$135.29^{+1.83}_{-1.83}$
EW $_{\text{HeI}\lambda 10830}$ emission narrow (Å)	$16.42^{+0.31}_{-0.31}$
$f_{\text{Pa}\gamma}$ emission (10 $^{-17}$ erg s $^{-1}$ cm $^{-2}$ )	$1.66^{+0.04}_{-0.04}$
FWHM $_{\text{Pa}\gamma}$ broad (km s $^{-1}$ )	$2552.62^{+55.41}_{-55.41}$
FWHM $_{\text{Pa}\gamma}$ narrow (km s $^{-1}$ )	$1194.92^{+32.95}_{-32.95}$
EW $_{\text{Pa}\gamma}$ emission broad (Å)	$41.67^{+0.79}_{-0.79}$
EW $_{\text{Pa}\gamma}$ emission narrow (Å)	$1.19^{+0.02}_{-0.02}$
EW $_{\text{HeI}\lambda 10830}$ absorption (Å)	$30.54^{+5.87}_{-5.87}$
$\log N(\text{He I}\lambda 10830)$ (cm $^{-2}$ )	$13.86^{+0.05}_{-0.05}$
cid_947	
RA, DEC	150.29725, 2.14884
Redshift	3.328
$\log L_{X,2-10 \text{ keV}}$ (erg s $^{-1}$ )	44.62
$\log L_{\text{bol}}$ (erg s $^{-1}$ )	46
$\log N_{\text{H}}$ (cm $^{-2}$ )	$23.47^{+0.29}_{-0.47}$
$\log M_{*}/M_{\odot}$	$11.01^{+0.19}_{-0.20}$
$\log \text{SFR}$ (M $_{\odot}$ yr $^{-1}$ )	$1.49^{+0.20}_{-0.20}$
$\log M_{\text{BH}}/M_{\odot}$	$9.84^{+0.28}_{-0.28}$
$\lambda_{\text{Edd}}$	$0.013^{+0.006}_{-0.006}$
$f_{\text{HeI}\lambda 10830}$ emission (10 $^{-17}$ erg s $^{-1}$ cm $^{-2}$ )	$1.90^{+0.06}_{-0.06}$
FWHM $_{\text{HeI}\lambda 10830}$ broad (km s $^{-1}$ )	$2473.41^{+49.28}_{-49.28}$
FWHM $_{\text{HeI}\lambda 10830}$ narrow (km s $^{-1}$ )	$1197.51^{+38.38}_{-38.38}$
EW $_{\text{HeI}\lambda 10830}$ emission broad (Å)	$74.50^{+2.38}_{-2.38}$
EW $_{\text{HeI}\lambda 10830}$ emission narrow (Å)	$4.75^{+0.15}_{-0.15}$
$f_{\text{Pa}\gamma}$ emission (10 $^{-17}$ erg s $^{-1}$ cm $^{-2}$ )	$0.67^{+0.02}_{-0.02}$
FWHM $_{\text{Pa}\gamma}$ broad (km s $^{-1}$ )	$4353.17^{+139.54}_{-139.54}$
FWHM $_{\text{Pa}\gamma}$ narrow (km s $^{-1}$ )	$1195.61^{+38.32}_{-38.32}$
EW $_{\text{Pa}\gamma}$ emission broad (Å)	$23.75^{+0.76}_{-0.76}$
EW $_{\text{Pa}\gamma}$ emission narrow (Å)	$5.45^{+0.17}_{-0.17}$
EW $_{\text{HeI}\lambda 10830}$ absorption (Å)	$32.52^{+10.32}_{-10.32}$
$\log N(\text{He I}\lambda 10830)$ (cm $^{-2}$ )	$14.05^{+0.21}_{-0.21}$

based on their hard X-ray detections and X-ray inferred hydrogen column densities.

#### 2.4.2. UV–mid-IR

For the bands not covered by the JWST imaging data, we collect the UV-to-mid-IR photometry using the Kron AUTO measurements from the COSMOS2020 Classic catalog **COSMOS2020** (J. R. Weaver et al. 2022), spanning from the *GALEX*/FUV band to the *Spitzer*/IRAC channel 4. The *u* band photometry is from the CFHT Large Area U band Deep Survey (CLAUDS) program (M. Sawicki et al. 2019). The ongoing HSC Subaru Strategic Program (HSC-SSP) survey provides imaging from *g* band to *y* band (H. Aihara et al. 2018). Besides, we include the HST/F814W photometry from A. Leauthaud et al. (2007). The HST/F814W AB magnitudes are  $24.49 \pm 0.05$  and  $20.50 \pm 0.01$  for **cid\_414** and **cid\_947**, respectively. The *YJHK<sub>s</sub>* data is from the fourth data release of the UltraVISTA survey (H. J. McCracken et al. 2012). For mid-IR photometry, we use the magnitudes from the Spitzer Large Area Survey with Hyper Suprime-Cam (SPLASH; C. L. Steinhardt et al. 2014). Neither of the two objects are detected in the *GALEX*/FUV or NUV bands.

#### 2.4.3. submm–FIR–radio

The **cid\_414** has been observed in multiple ALMA programs, including #2016.1.01001.S (PI: J. Kartaltepe; 887 s integration time in Band 3), #2021.1.01328.S (PI: W. Rujopakarn; 60 s in Band 7), #2021.1.00225.S (PI: C. Casey; 45 s in Band 4), and #2023.1.00180.L (CHAMPS; PI: A. Faisst; Faisst et al., in prep.; 54 s in Band 6). There is no  $> 3\sigma$  dust continuum detection in the Band 3, 6 and 7 observation for **cid\_414**. The **cid\_947** has a reliable (S/N  $\sim 7.5$ ) ALMA Band 6 (1.1 mm) detection from program #2016.1.01012.S (PI E. Treister). We retrieved the reduced data from the latest public release of the A3COSMOS program (D. Liu et al. 2019).

We match the FIR photometry of these two sources using the super-deblended catalog (S. Jin et al. 2018), which combines FIR to (sub)millimeter measurements in the COSMOS field. The Herschel/PACS 100 and 160  $\mu\text{m}$  data are from the PEP program (PI D. Lutz; D. Lutz et al. 2011), and the SPIRE 250, 350, and 500  $\mu\text{m}$  data are from the Herschel Multi-tiered Extragalactic Survey (PI: S. Oliver; S. J. Oliver et al. 2010). Since the super-deblended catalog is based on NIR prior positions, we adopt a matching radius of 1 arcsec. Neither source has S/N  $> 3$  detections at 100 or 160  $\mu\text{m}$ .

At radio wavelengths, we search the VLA-COSMOS 1.4 GHz (E. Schinnerer et al. 2010) and 3 GHz (V. Smolčić et al. 2017) catalogs. The **cid\_414** is detected

with high significance ( $S/N > 10$ ) at both 1.4 GHz and 3 GHz, while **cid\_947** shows no radio detection.

#### 2.4.4. Ground-based spectroscopy

We find that **cid\_414** has archival Keck/LRIS (exptime = 2h,  $R \sim 1100$ ) spectroscopy from the COSMOS Lyman-Alpha Mapping and Tomography Observations (CLAMATO) survey (K.-G. Lee et al. 2018), covering 3200–5500 Å, and Keck/DEIMOS (exptime = 1800s) spectroscopy from the DEIMOS 10k survey (G. Hasinger et al. 2018), covering 5500–9800 Å and spectral resolution  $R \sim 2000$ . The two parts of the spectra are shown in the Appendix Figure A2. A clear Ly $\alpha$  emission line is detected at  $z = 2.933$  with a signal-to-noise ratio of  $\sim 45$ , while no C IV or C III] lines are detected. The Ly $\alpha$  line is well fitted by a Gaussian profile with a FWHM of  $744.90 \pm 32.52$  km s $^{-1}$ . The apparent Ly $\alpha$  luminosity is  $10^{42.49}$  erg s $^{-1}$ . This value is similar to that detected in a sample of 23  $z \sim 2$  type II AGN selected from SDSS, part of which show both narrow Ly $\alpha$  and broad Balmer lines (B. Wang et al. 2025a).

The **cid\_947** was observed in the zCOSMOS-bright survey (S. J. Lilly et al. 2007), showing significant ( $\sim 12000$  km s $^{-1}$ ) blueshifted outflow features in the Si IV, C IV, and Al III absorption lines (see the right panel of Figure A2). B. Trakhtenbrot et al. (2015) also obtained a  $K$ -band (1.9–2.4  $\mu$ m) spectrum of this target with Keck/MOSFIRE. The spectrum shows a broad H $\beta$  line with FWHM = 11330 km s $^{-1}$ , yielding a black hole mass estimate of  $6.91 \times 10^9 M_\odot$  from the broad-line virial method.

### 3. MEASUREMENTS AND PROPERTIES

#### 3.1. Emission and absorption line measurements

We present the NIRCam F444W imaging, and the 2D (without continuum subtraction) and 1D grism spectra of **cid\_414** and **cid\_947** in Figure 1. For the two targets, we first fit the He I+Pa $\gamma$  line structure using Gaussian profiles for both the emission and absorption components. A linear continuum is fitted around the emission lines in the rest-frame wavelength ranges 1.02–1.05  $\mu$ m and 1.11–1.14  $\mu$ m. We fit the He I $\lambda$ 10830 and Pa $\gamma$  emission lines using three models: broad only, narrow only, and broad+narrow components, and we find that the resulting  $\chi^2$  values are similar. In Figure 1, we present the fitting results for the two targets using a model with one broad and one narrow component. We describe the details of the emission and absorption line measurements of the two targets below and in Table 1.

##### 3.1.1. **cid\_414**

For **cid\_414**, we fix the center of the He I $\lambda$ 10830 and Pa $\gamma$  lines to the redshift determined from the Ly $\alpha$  line

( $z = 2.933$ , vertical dashed line in Figure 1). The FWHM of the broad (narrow) component of **cid\_414** is  $3591.15 \pm 77.87$  ( $1192.77 \pm 32.18$ ) km s $^{-1}$  for the He I $\lambda$ 10830 line. The line widths for the Pa $\gamma$  are  $2552.62 \pm 55.41$  and  $1194.92 \pm 32.95$  km s $^{-1}$  for the broad and narrow components, respectively. We correct the line instrumental broadening based on the NIRCam grism line-spread function (T. P. Greene et al. 2017). The equivalent widths (EWs) of the He I $\lambda$ 10830 and Pa $\gamma$  broad emission lines are  $135.29 \pm 1.83$  Å and  $16.42 \pm 0.31$  Å, respectively.

Considering the possible saturation of the absorption lines, we use the apparent optical depth (AOD) method to estimate the column density of the He I $\lambda$ 10830 absorption line. The optical depth is defined as  $\tau(v) = -\ln(I(v)/I_c(v))$ , where  $I(v)$  and  $I_c(v)$  are the observed spectral intensity and the interpolated absorption-free continuum, respectively. The column density is then calculated by integrating the optical depth over the velocity range of the absorption:

$$N = \frac{m_e c}{\pi e^2 \lambda f} \int_{v_{\min}}^{v_{\max}} \tau(v) dv, \quad (1)$$

where  $m_e$  and  $e$  are the electron mass and charge,  $c$  is the speed of light,  $\lambda$  is the rest-frame transition wavelength, and  $f$  is the oscillator strength. We obtain for **cid\_414** a column density of  $\log N(\text{He I}\lambda 10830)/\text{cm}^{-2} = 13.86 \pm 0.05$ .

#### 3.1.2. **cid\_947**

Different from **cid\_414**, where the He I $\lambda$ 10830 absorption does not show a significant velocity offset from the emission-line center, the object **cid\_947** is a BAL quasar exhibiting a significant velocity offset ( $> 5000$  km s $^{-1}$ ) in the absorption features in both the rest-frame UV lines and He I $\lambda$ 10830. The fluxes of He I $\lambda$ 10830 and Pa $\gamma$  emission lines for **cid\_947** are  $(1.90 \pm 0.06) \times 10^{-17}$  and  $(0.67 \pm 0.02) \times 10^{-17}$  erg s $^{-1}$  cm $^{-2}$ , respectively. From the right panel of Figure A2, we see that the He I $\lambda$ 10830 line profile shares a similar velocity width with the rest-frame UV absorption lines. We fit the He I $\lambda$ 10830 absorption with three major components, and list the corresponding measured equivalent widths (as comp1,2,3) and the total column density in Table 1. There is likely a fourth subcomponent at a velocity offset of  $\Delta v \sim -12,000$  km s $^{-1}$ , but since it is not detected above  $3\sigma$  in the 2D spectra, we do not include it when calculating the He I $\lambda$ 10830 absorption-line column density.

#### 3.2. JWST photometry

For all JWST NIRCam and MIRI bands used in this study, we performed photometric measurements

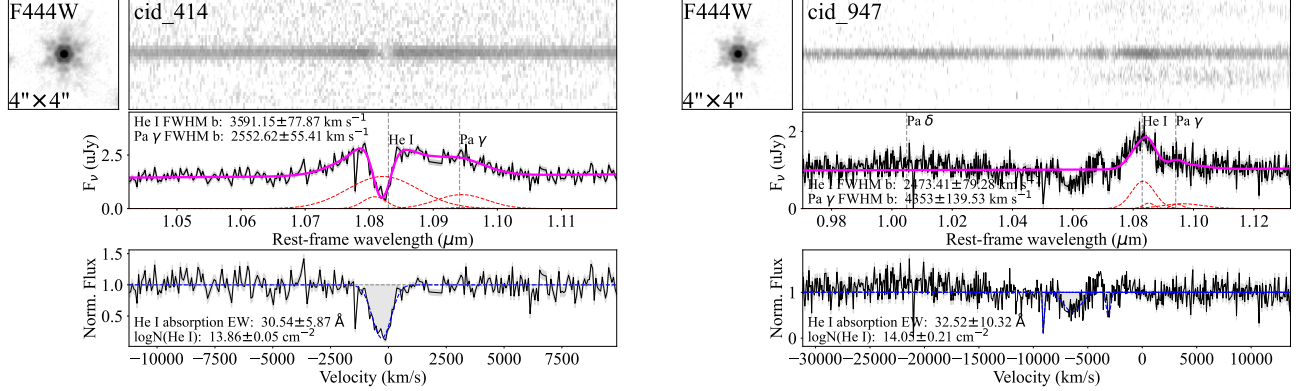


**Figure 1.** The JWST 2D and 1D grism F444W spectra of `cid_414` (left) and `cid_947` (right) from C3D. The Gaussian fits to the He I $\lambda$ 10830 - Pa $\gamma$  complex are shown as red solid curves. The broad and narrow components of the fits are plotted as red dashed curves.

using SEP for source detection and SE++ for photometry (E. Bertin et al. 2020). SEP was applied to the square root of a positive  $\chi^2$  detection image constructed from all available broadband images within each tile. It was run in both “hot” and “cold” modes, which were later merged to optimize the detection of bright, extended galaxies and deblended faint, compact sources. Automatic Kron photometry was carried out using “small Kron” ( $k=1.2$ ,  $R=1.6$ ) and “default Kron” ( $k=2.5$ ,  $R=3.5$ ) apertures with SEP and `photutils`, and the ratio of these fluxes was used for aperture correction. The images are not point-spread-function (PSF)-matched; however, the Kron shape parameters are derived from the  $\chi^2$  image. SE++ was subsequently run in ASSOC mode to compute fixed-aperture photometry for the SEP-detected sources. The complete C3D photometry details and catalog will be described in Champagne et al., in prep.

### 3.3. Point-Spread Function Construction and Image Decomposition

In order to measure the host galaxy (if present) properties, we perform careful imaging decomposition. Previous studies usually adopt two components to model the light distribution: a PSF profile for the AGN and a Sérsic profile for the host galaxy (X. Ding et al. 2020; J. Li et al. 2021; X. Ding et al. 2022; M.-Y. Zhuang & Y. Shen 2024). The PSF is constructed from stars within a  $2''$  radius around the targets. We use 11 stars for `cid_414` and 5 for `cid_947`. The stellar cutouts are oversampled by a factor of three, recentered, and median stacked to generate the final PSF.

We use `SExtractor` to identify stellar candidates in each tile and band, excluding sources near image edges or affected by bad pixels. From the remaining objects, we select stars with consistent half-light radii and ex-

tract  $6''$  cutouts, within which  $\sim 98\%$  of the stellar light is enclosed (M.-Y. Zhuang et al. 2024). The `SExtractor` segmentation map masks unrelated sources.

We then perform the image decomposition using the code `GALFITS` (R. Li et al. 2025). Different from traditional single-band decomposition tools, `GALFITS` simultaneously fits images taken in multiple bands and incorporates physically motivated SED models into the fitting process. This enables the simultaneous extraction of the physical properties of both the AGN and the host galaxy. As shown in Figure A3, `cid_947` appears morphologically consistent with a point source, while `cid_414` exhibits asymmetric structures in the JWST F115W, F150W, and F200W bands. About  $\sim 51\%$  of the total flux is enclosed within a  $0''.18$  aperture in F200W (82% for `cid_947`). The F200W emission extends to  $\sim 7.9$  pkpc to the north. This extension may trace H $\beta$ +[O III] emission in F200W and Mg II+[O II] emission in F115W/F150W (Fu et al. submitted). For `cid_947`, a single Sérsic plus PSF model yields a stellar mass of  $10^{10.94} M_\odot$ . We find that if we include the extended region and fit `cid_414` with a single Sérsic component, the derived stellar mass is  $10^{11.83} M_\odot$ , comparable to that of a very massive quiescent galaxy in the local universe. We therefore adopt two Sérsic components to model the host galaxy emission of `cid_414`, without imposing constraints on the Sérsic index or effective radius because of its asymmetric morphology. We exclude the flux from the second Sérsic component when estimating the host galaxy mass and in the subsequent SED fitting in Section 3.4. The stellar mass derived from the primary Sérsic component is  $10^{11.12\pm0.33} M_\odot$ . For a detailed decomposition of the two components, we refer to Fu et al. (submitted), where the second component is interpreted as nebular emission.

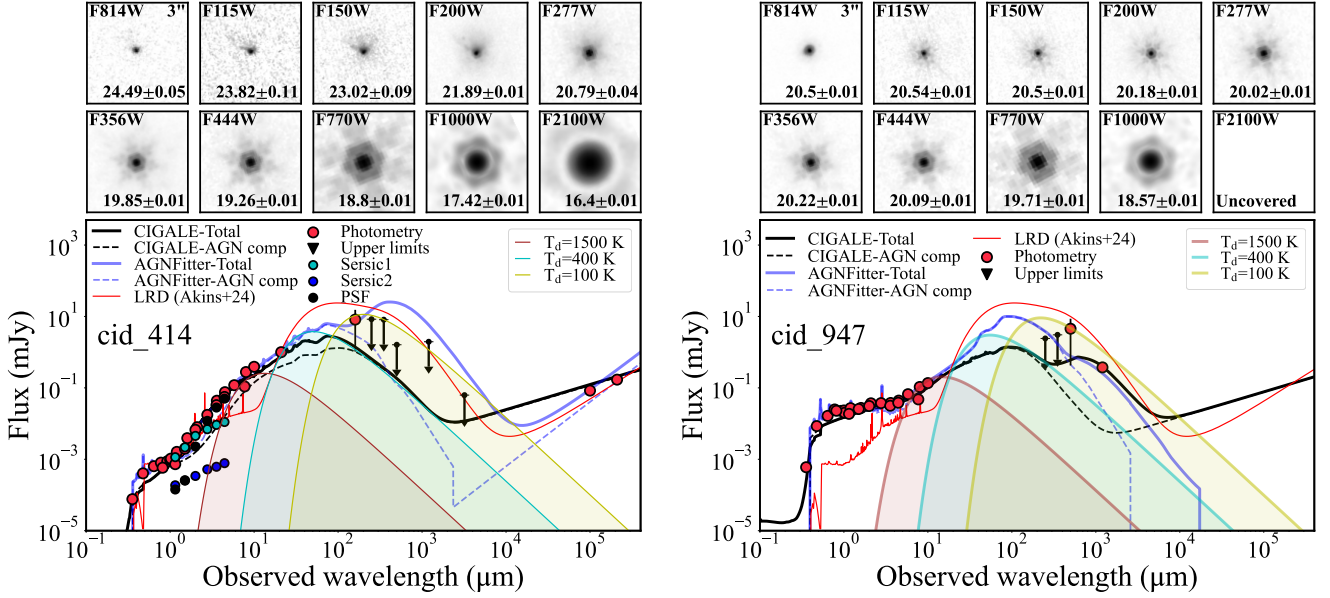


**Figure 2.** Multiwavelength images and SED fitting results of **cid\_414** (left) and **cid\_947** (right). We present the SED fitting from two tools, **AGNfitter** (blue lines) and **CIGALE** (black lines), respectively. The dashed lines represent the best-fit AGN emission. Red dots with error bars indicate the observed photometry, while black arrows show the upper limits. For **cid\_414**, the green, blue, and black points show the model photometry from the two Sérsic components, as plotted in Figure A3. The details of the host galaxy decomposition are presented in Section 3.3.

### 3.4. SED fitting and host galaxy properties

To measure the host galaxy and black hole properties of the two targets, we perform multiwavelength spectral energy distribution (SED) fitting using UV-to-radio photometry introduced in Section 2. To mitigate systematics arising from the assumptions built into any single SED fitting tool (choices of AGN and stellar components, dust treatment, and star formation history etc), we use two independent codes, **CIGALE** (M. Boquien et al. 2019) and **AGNfitter** (L. N. Martínez-Ramírez et al. 2024). **CIGALE** fits the SED with energy balance, adopting BC03 stellar models (G. Bruzual & S. Charlot 2003), a Chabrier IMF (G. Chabrier 2003), a delayed-exponential star formation history (SFH), the D. Calzetti et al. (2000) attenuation law, B. T. Draine et al. (2014) dust emission, and the SKIRTOR AGN model (M. Stalevski et al. 2012, 2016). **AGNfitter** uses the same stellar and attenuation models but does not enforce energy balance; it models dust emission with C. Schreiber et al. (2018) templates and decomposes AGN emission into an accretion-disk big blue bump (BBB) component (M. J. Temple et al. 2021) and a dusty torus described by the CAT3D library (S. F. Höning & M. Kishimoto 2017).

The best-fit SEDs from **CIGALE** and **AGNfitter** are shown in black and blue in Figure 2, respectively. In the **AGNfitter** results, the rest-frame UV to mid-IR

emission of both targets is dominated by the AGN. In the **CIGALE** results, **cid\_947** is AGN-dominated, while **cid\_414** shows a non-negligible contribution from stellar emission. In particular, if we include the fluxes from both Sérsic components for **cid\_414**, the derived stellar masses are  $10^{12.09} M_{\odot}$  and  $10^{12.08} M_{\odot}$  from **CIGALE** and **AGNfitter**, respectively, which are unrealistically high for a typical star-forming galaxy at  $z \sim 3$ . We therefore adopt only the Sérsic 1 component in the SED fitting, resulting in a stellar mass of  $\sim 10^{11.12 \pm 0.33} M_{\odot}$ . We further use the F200W (rest frame V band) Sérsic 1 flux and the mass-to-light ratio from S. M. Faber & J. S. Gallagher (1979), varying the  $M/L$  from 2 to 7.6 as a consistency check, yielding a stellar mass of  $10^{10.92 \pm 0.29} M_{\odot}$ , as listed in Table 1.

For both the **CIGALE** and **AGNfitter** fitting results, **cid\_414** shows a relatively higher star formation rate (SFR) than **cid\_947**, as listed in Table 1. We plot the star-forming main sequence in the  $M_*$ -SFR plane in Figure 3. Our measurements reveal that **cid\_414** lies on the star-forming main sequence at  $z \sim 3$ , while **cid\_947** is slightly below the relation.

### 3.5. Black hole mass and Eddington ratio measurements

Since we do not have archival observations of broad Balmer lines or Mg II for **cid\_414**, which are typically used to estimate the black hole mass in type I AGNs at

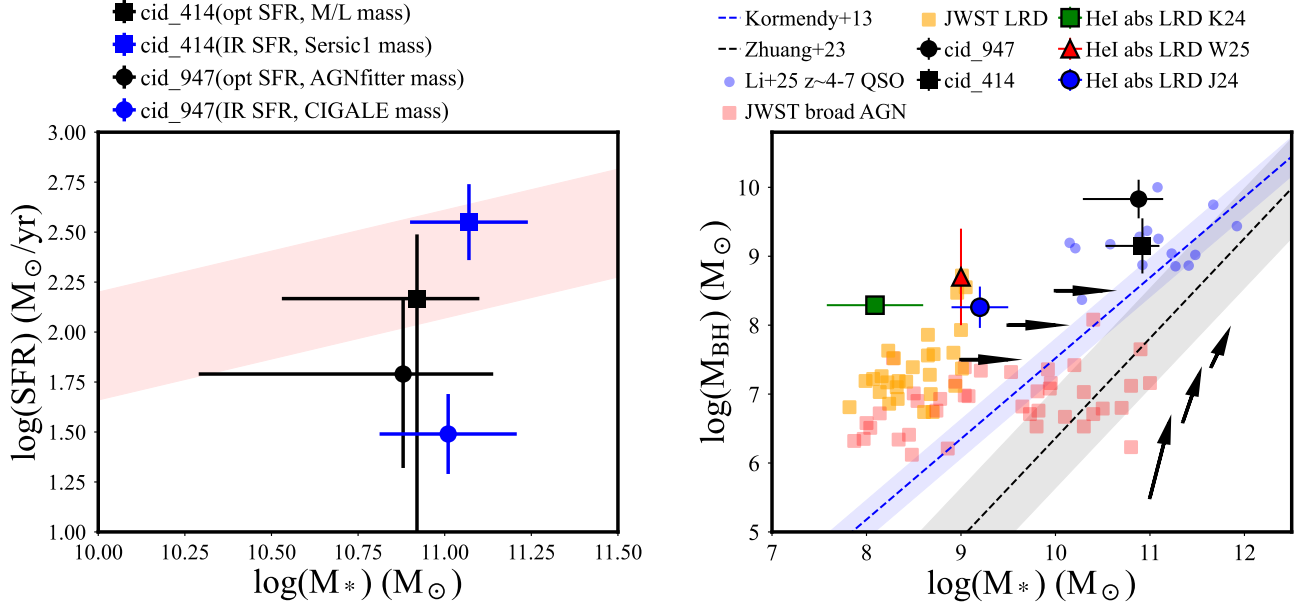


**Figure 3.** *Left:* Host galaxy star formation rate (SFR) and stellar mass ( $M_*$ ) from SED fitting (squares: **cid\_414**; circles: **cid\_947**). The pink shaded region indicates the star-forming main sequence from K. E. Whitaker et al. (2012). *Right:* Stellar mass versus black hole mass. The local relations from J. Kormendy & L. C. Ho (2013) and M.-Y. Zhuang & L. C. Ho (2023) are shown as blue and black dashed lines, with their corresponding  $1\sigma$  shaded regions. The black arrows indicate the two black hole–host galaxy growth pathways proposed in M.-Y. Zhuang & L. C. Ho (2023). Blue symbols mark high-luminosity quasars at  $z \sim 6$  from R. Li et al. (2025), including sources from ASPIRE (PID #2078, PI: F. Wang), EIGER (PID #1243, PI: S. Lilly), and the Subaru High-redshift Exploration of Low-luminosity Quasars survey. The squares represent the JWST AGN compilation (B. L. Jones et al. 2025), with LRDs in orange and non-LRDs in red. Three additional AGNs with He I  $\lambda 10830$  absorption from the literature are also shown: RUBIES 40579 (D. D. Kocevski et al. 2025), W25 (B. Wang et al. 2025b), and J25 (I. Juodžbalis et al. 2024).

similar redshifts in the literature, we instead adopt an indirect empirical scaling relation based on the He I and H $\beta$  lines, as calibrated from the local BASS sample (F. Ricci et al. 2017):

$$\log\left(\frac{M_{\text{BH}}}{M_{\odot}}\right) = a + b \left[ 2 \log\left(\frac{\text{FWHM}}{10^4}\right) + 0.5 \log\left(\frac{L_X}{10^{42}}\right) \right], \quad (2)$$

where  $a = 8.19$ ,  $b = 1.38$  and  $L_X$  is the 2-10 keV luminosity. We then derive black hole masses of  $\log(M_{\text{BH}}/M_{\odot}) = 9.15 \pm 0.40$  for **cid\_414**. The uncertainties are from the measurement errors on the He I  $\lambda 10830$  FWHM and the intrinsic scatter of the calibration. For **cid\_947**, we adopt the black hole mass estimated from the broad H $\beta$  line, following the method described in B. Trakhtenbrot et al. (2015). The X-ray bolometric luminosities of the two targets are converted from the 2 to 10 keV luminosity using the bolometric correction factor  $K_X = L_{\text{bol}}/L_X$  from F. Duras et al. (2020):

$$K_X = 15.33 \left[ 1 + \left( \frac{\log(L_{X,2-10 \text{ keV}}/L_{\odot})}{11.48} \right)^{16.20} \right]. \quad (3)$$

We then derive the Eddington ratio as

$$\lambda_{\text{Edd}} = \frac{L_{\text{bol}}}{1.26 \times 10^{38} (M_{\text{BH}}/M_{\odot})}. \quad (4)$$

The resulting Eddington ratios are  $\lambda_{\text{Edd}} = 0.28^{+0.41}_{-0.18}$  for **cid\_414** and  $\lambda_{\text{Edd}} = 0.013^{+0.01}_{-0.01}$  for **cid\_947**.

## 4. DISCUSSION

### 4.1. Dense Gas in Different SMBH Growth Phase

To examine the role of dense absorbing gas in AGN obscuration and in the growth of black holes and their hosts, we first compare the observed properties of the two targets. We note that **cid\_414** shows higher X-ray luminosity and SFR but lower  $N_{\text{H}}$ ,  $N_{\text{HeI}\lambda 10830}$ , and black hole mass than **cid\_947**, suggesting that obscuring gas and dust may trace different stages of black hole and host-galaxy growth.

In Figure 3, we show the relation between black hole mass and host stellar mass, together with the reference relations from M.-Y. Zhuang & L. C. Ho (2023) (black dashed line) and J. Kormendy & L. C. Ho (2013) (blue dashed line). M.-Y. Zhuang & L. C. Ho (2023) suggested two co-evolutionary pathways: galaxies above

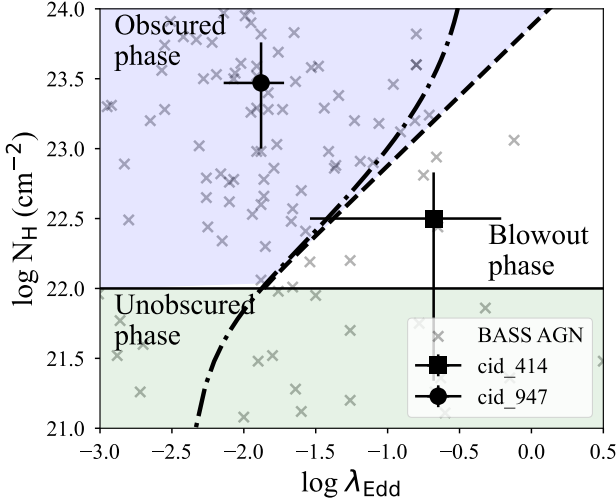


**Figure 4.** X-ray-inferred hydrogen column density versus Eddington ratio. The dashed and dash-dotted curves show the effective Eddington limits for the single-scattering case (A. C. Fabian et al. 2009) and for models including IR radiation trapping (W. Ishibashi et al. 2018), respectively. The blue shaded region marks the obscured regime, while the green shaded region indicates unobscured AGNs. The white region represents the blowout phase where AGN radiative feedback is expelling the surrounding dusty gas.

the  $M_{\text{BH}}-M_*$  relation tend to grow their stellar mass further, while those below it may undergo rapid black hole growth. Both of our targets lie above the empirical relation derived from local AGN samples. **cid\_414** has a higher  $\lambda_{\text{Edd}}$  and lies closer to the relation, consistent with concurrent star formation and rapid black hole growth. Meanwhile, the low  $\lambda_{\text{Edd}}$  and prominent outflows in **cid\_947** suggest a more evolved phase in which AGN feedback is suppressing star formation. Its ALMA detection further hints that star formation may dominate in the next stage. B. Trakhtenbrot et al. (2015) argued that the black hole in **cid\_947** is overmassive relative to systems at similar redshifts, implying that much of its black hole growth may have occurred in an earlier episode.

We plot the limited sample of LRDs exhibiting He I $\lambda$ 10830 absorption (B. Wang et al. 2025b; D. D. Kocevski et al. 2025; I. Juodžbalis et al. 2024) at  $z \sim 3$  together with all JWST detected AGNs, including LRDs, from B. L. Jones et al. (2025) in the right panel of Figure 3. We find that **cid\_947** and the LRDs showing prominent blueshifted He I $\lambda$ 10830 broad line outflows have higher black hole masses than other LRDs and AGNs at similar stellar masses, suggesting that they are undergoing rapid black hole growth accompanied by strong AGN driven feedback during both early and later evolutionary phases. We remain cautious about the black hole mass

estimates in LRDs because they may be overestimated if a bolometric luminosity correction is required (J. E. Greene et al. 2025). Nevertheless, current observations and theoretical expectations still support a scenario of super Eddington accretion in these systems.

We then discuss the differences in the dense absorbing gas and overall obscuration between the two targets. In the analysis of 836 local X-ray AGN presented in C. Ricci et al. (2017b), the authors concluded that the mass-normalized accretion rate, that is, the  $\lambda_{\text{Edd}}$ , is likely the key parameter regulating nuclear obscuration. In their Figure 4, among Compton-thin sources ( $22.0 < \log N_{\text{H}}/\text{cm}^{-2} < 24$ ), when  $\lambda_{\text{Edd}}$  exceeds approximately 0.05, the covering factor of dusty gas decreases from about 0.8 to about 0.3. Both of our targets are classified as Compton-thin objects based on their X-ray-inferred  $N_{\text{H}}$ . The dusty gas covering factor is then estimated to be 0.85 for **cid\_947** and < 0.2 for **cid\_414**, respectively. This difference is interpreted as the result of increasing radiation pressure in high- $\lambda_{\text{Edd}}$  systems that clears obscuring material along the line of sight. We also show the relation between  $N_{\text{H}}$  and  $\lambda_{\text{Edd}}$  for our sources in Figure 4. The source **cid\_947** lies in an obscured phase, whereas **cid\_414** is located in the blowout phase, in which long-lived dusty gas clouds cannot be sustained due to strong radiation pressure from the AGN. This further supports the scenario that **cid\_414** is undergoing rapid black hole growth.

We further estimate the physical properties (volume density, column density, ionization parameter, and geometry) of the dense absorber around the nuclear region by modeling its photoionization state using CLOUDY C25.00 (C. M. Gunasekera et al. 2025). In the modeling, we adopt an incident radiation field composed of the extragalactic UV background and an AGN continuum (W. G. Mathews & G. J. Ferland 1987). We vary the ionization parameter  $\log U$ , metallicity  $Z/Z_{\odot}$ , and gas density  $n_{\text{H}}/\text{cm}^{-3}$  in the models. The ionization parameter  $\log U$  is defined as

$$U = \frac{Q}{4\pi r^2 n_{\text{H}} c}, \quad (5)$$

where  $Q$  is the ionizing photon emission rate. We set  $\log U$  to vary within the range  $-4 \leq \log U \leq 2$ , and gas density within  $2 \leq \log n_{\text{H}} \leq 10$ . The stopping column density  $N_{\text{H}}$  is fixed to the lower limit of the observed value. We plot  $\log N_{\text{HeI}}$  as a function of  $\log U$ ,  $\log n_{\text{H}}$  and  $\log(Z/Z_{\odot})$  in Figure 5. We find the best-match values of  $\log U$  and  $\log n_{\text{H}}/\text{cm}^{-3}$  to reproduce the observed He I $\lambda$ 10830 column densities are  $\log U = -1$ ,  $\log n_{\text{H}} = 10$  for the **cid\_414** and  $\log U = 0$ ,  $\log n_{\text{H}} = 9$  for the **cid\_947**. We also find that when the gas is dense enough to reproduce the observed He I $\lambda$ 10830 column

densities, adopting 0.1 or 1  $Z_{\odot}$  does not significantly affect the modelling results. The inferred dense gas density is consistent with the values predicted for LRDs in K. Inayoshi & R. Maiolino (2025).

#### 4.2. Dust torus and dense absorbing gas geometry

Given the MIRI detections at  $\geq 10$ – $20$   $\mu\text{m}$  and the constraints from the photoionization modelling, we tentatively explore the geometry of the AGN-heated dust and the dense absorbing gas. In the SED fitting (Figure 2), we include dust components modeled as black-bodies with temperatures of 1500, 400, and 100 K. For **cid\_414**, the MIRI fluxes between 10 and 21  $\mu\text{m}$  are well reproduced by a  $\sim 1500$  K component, while **cid\_947** shows a slightly lower hot-dust temperature. Together with the prominent outflow signatures, these results suggest that **cid\_414** is experiencing strong AGN feedback associated with rapid SMBH growth.

The geometry of the dense absorbing gas is likely complex, and our discussion below provides only a simplified estimate. Under a single-slab assumption, the absorber thickness is  $l = N_{\text{H}}/n_{\text{H}}$ , giving  $l \sim 10^{-6}$  pc for **cid\_414** and  $l \sim 10^{-4}$  pc for **cid\_947**. The distance between the absorber and the ionizing source is estimated using the ionization parameter:

$$r = \sqrt{\frac{L_{\text{bol}} f_{\text{ion}}}{4\pi n_{\text{H}} c U \langle h\nu_{\text{ion}} \rangle}}, \quad (6)$$

where  $f_{\text{ion}}$  and  $\langle h\nu_{\text{ion}} \rangle$  are determined by the AGN SED (W. G. Mathews & G. J. Ferland 1987). Using our best-fitting values of  $U$ , we obtain  $r \approx 0.02$  pc for **cid\_414** and  $r \approx 0.04$  pc for **cid\_947**. Combined with the ionization parameter and density inferred from the CLOUDY modelling, the dense gas in **cid\_414** likely resides very close to the nucleus with a small covering factor. This dense material remains in the line of sight, producing absorption on top of the emission lines even as the system enters a blowout phase. For **cid\_947**, the absorbing gas probably resides near the outer BLR, tracing multiple outflowing clumps. These clouds are strongly heated by the AGN radiation field, which lowers the total hydrogen density and produces a higher ionization parameter.

Assuming thermal equilibrium, the inner radius of the dusty torus is

$$R_{\text{torus}} = \sqrt{\frac{L_{\text{bol}}}{4\pi\sigma T^4}}, \quad (7)$$

where  $\sigma$  is the Stefan–Boltzmann constant and we adopt a dust sublimation temperature of  $T = 1500$  K (e.g., S. Zhang et al. 2015), yielding  $R_{\text{torus}} \approx 1.19$  pc for **cid\_414** and  $R_{\text{torus}} \approx 0.54$  pc for **cid\_947**. Consid-

ering the uncertainty in  $L_{\text{bol}}$  converted from the X-ray 2–10 keV luminosity, we also adopt the  $L_{\text{bol}}$  estimated from the SED fitting described in Section 3.4. This yields  $R_{\text{torus}} = 0.86$ – $1.19$  pc for **cid\_414** and 0.54– $0.96$  pc for **cid\_947**. The absorber thickness and distance are smaller than the torus scale and comparable to the BLR size (I. Juodžbalis et al. 2024), implying that the absorbing gas lies at BLR-like radii, shares the BLR kinematics, and is influenced by the obscuration geometry of the hot dust torus.

#### 4.3. Luminosity function and comparison with other AGN populations

Given the rarity of He I  $\lambda 10830$  absorption detected in high-redshift AGNs in the past, mainly because of the limitations of ground-based instruments, we further compare this population of X-ray and MIRI bright AGNs with dense absorbing gas to other populations, including type I quasars, X-ray selected AGNs, and LRDs.

With the F444W grism spectral coverage, we are able to detect He I  $\lambda 10830$  at redshifts  $z = 2.7$ – $3.6$ . Besides the two targets analyzed in this work, there are two additional sources in the C3D coverage that exhibit He I  $\lambda 10830$  absorption and MIRI detections (one reported in S. Fu et al., submitted, and another with very weak He I  $\lambda 10830$  absorption,  $\log N_{\text{HeI}} < 12.0$ ). We do not present them in this work because they did not have secure spectroscopic redshifts prior to the C3D observations, which excludes them based on our selection criteria described in Section 2. We plot the loosely constrained luminosity function (LF) of the two AGNs at  $z \sim 3$  in Figure 6, and the LF including the two additional sources is indicated by the black dashed line. We estimate the luminosity density  $\Phi$  following F. Sun et al. (2023) as  $\Phi = N_{\text{src}}/(V_{\text{max}} \text{d} \log L)$ , where  $N_{\text{src}}$  is the number of objects in the luminosity bin,  $\text{d} \log L$  is the bin width, and  $V_{\text{max}}$  is the comoving volume (in  $\text{Mpc}^{-3}$ ) within the redshift interval  $z = 2.7$ – $3.6$  and the  $0.14 \text{ deg}^2$  C3D MIRI coverage area. Since no previous He I  $\lambda 10830$  absorption X-ray AGN LF exists at  $z \sim 3$  and our selection in this work is not strictly complete, we do not apply any completeness correction. Instead, we treat the resulting LF as a lower limit and plot it in Figure 6. The abundance of AGNs with He I  $\lambda 10830$  absorption and mid-IR detections is about 0.7 dex lower than the predicted abundance of quasars with similar luminosities at  $z = 3$  (black dashed line; X. Shen et al. 2020), and about one dex lower than the LRD population at  $z = 5$ – $7$  (H. B. Akins et al. 2025).

In the pre-JWST era, broad absorption line (BAL) quasars accounted for 10–30% of the total quasar population (F. Shankar et al. 2008; P. Hiremath et al. 2025;

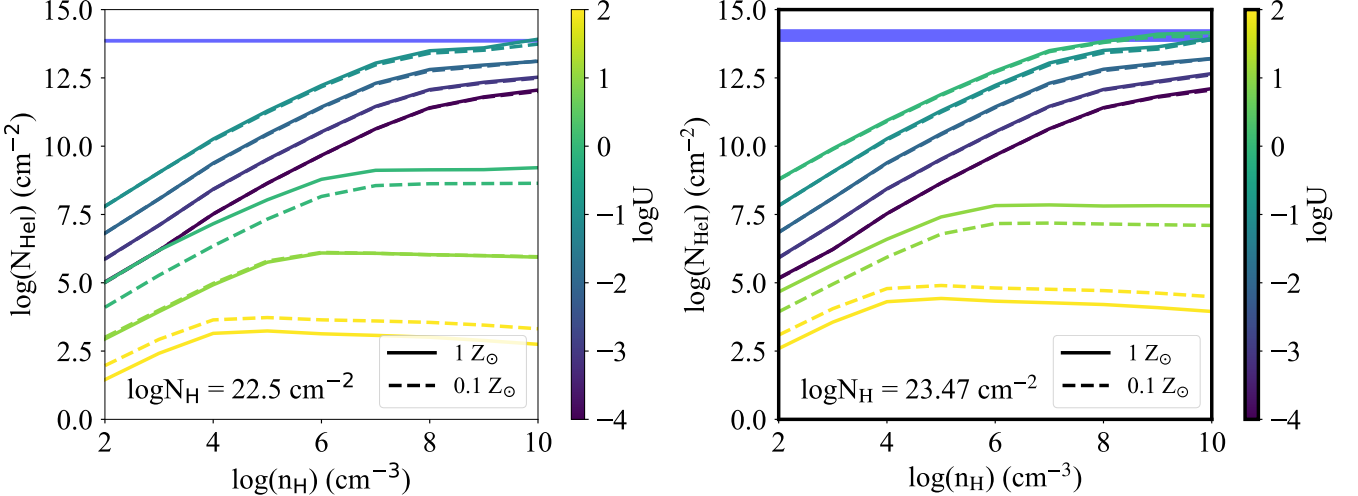


**Figure 5.** The column density of He I ( $\log N_{\text{HeI}}$ ) in the metastable level as a function of gas volume density from the CLOUDY modeling. The left panel shows `cid_414` and the right panel shows `cid_947`, each modeled with a different stopping criterion in  $N_{\text{H}}$ . Solid lines represent models with solar metallicity and the dashed lines represent models with  $\log(Z/Z_{\odot}) = -1$ . Colors indicate the value of  $\log U$ . The horizontal blue line marks the observed  $\log N_{\text{HeI}}$  for each source.

M. Vivek & D. Wylezalek 2025), and most identified BAL systems showed absorption in high-ionization transitions such as C IV and Si IV. JWST has now revealed more AGNs exhibiting He I $\lambda 10830$  and/or Balmer-line absorption at high redshift (R. Maiolino et al. 2024; J. Matthee et al. 2024). The fraction of LRDs with Balmer absorption at  $z = 4\text{--}6$  can reach 10–20% (X. Lin et al. 2024). We note that most current JWST spectra of LRDs with He I $\lambda 10830$  absorption have been obtained using the low-resolution prism, and the fraction of AGNs exhibiting such absorption may increase as higher-resolution spectroscopy becomes more widely available. Compared with the local X-ray AGN sample (BASS; T. T. Ananna et al. 2022), the abundance of He I $\lambda 10830$ -absorbing AGNs in our sample is higher, which may reflect the limited comoving volume probed at low redshift and the relative scarcity of high-luminosity AGNs in the nearby universe. However, our estimate is based on only two objects, and a larger sample is required to place stronger constraints on the luminosity function of absorption-line AGNs at this epoch.

## 5. SUMMARY

In this letter, we present two X-ray AGNs (`cid_414` and `cid_947`) with prominent He I $\lambda 10830$  absorption features at  $z \sim 3$  in the COSMOS field. The objects are selected from the COSMOS X-ray AGN catalog (S. Marchesi et al. 2016) and are required to be covered by the MIRI observations in the COSMOS-3D survey. A strong Ly $\alpha$  emission line is detected in `cid_414`, while rest-frame UV emission lines are absent in `cid_414`. In `cid_947`, the He I $\lambda 10830$  absorption shows a clear

blueshifted outflow signature, consistent with the outflow features seen in the C IV and Si IV lines.

We investigate the role of dense absorbing gas in AGN obscuration and black hole growth in these two systems. The source `cid_414` has a higher X-ray luminosity,  $\lambda_{\text{Edd}}$  and lower gas obscuration fraction, suggesting rapid black hole growth, while `cid_947` shows stronger cold dust emission, indicating that star formation may be suppressed by AGN feedback at this stage but could overcome this effect and re-emerge in the next phase. The observed differences in  $N_{\text{H}}$  and  $\lambda_{\text{Edd}}$  are consistent with an evolutionary sequence in which `cid_414` is in a blowout phase, where radiation pressure is clearing the obscuring gas, whereas `cid_947` remains in a more obscured phase. Photoionization modeling indicates that the dense absorbing gas is much smaller in scale than the dusty torus and likely resides near the outer region of the broad-line region. Together with the He I $\lambda 10830$  absorbing gas in LRDs detected at  $z \sim 3$ , we suggest that dense absorbing gas is plausibly common during periods of rapid black hole growth and may play a critical role in regulating AGN obscuration and the co-evolution of black holes and their host galaxies. A larger sample is needed to better constrain the luminosity function and to establish a more complete evolutionary picture of such absorption-line AGNs, including LRDs, at high redshift.

## ACKNOWLEDGEMENTS

ZJL and SZ acknowledge support from the Chinese Academy of Sciences (no. E5295401). JBC acknowledges funding from the JWST Arizona/Steward Postdoc in Early galaxies and Reionization (JASPER) Scholar

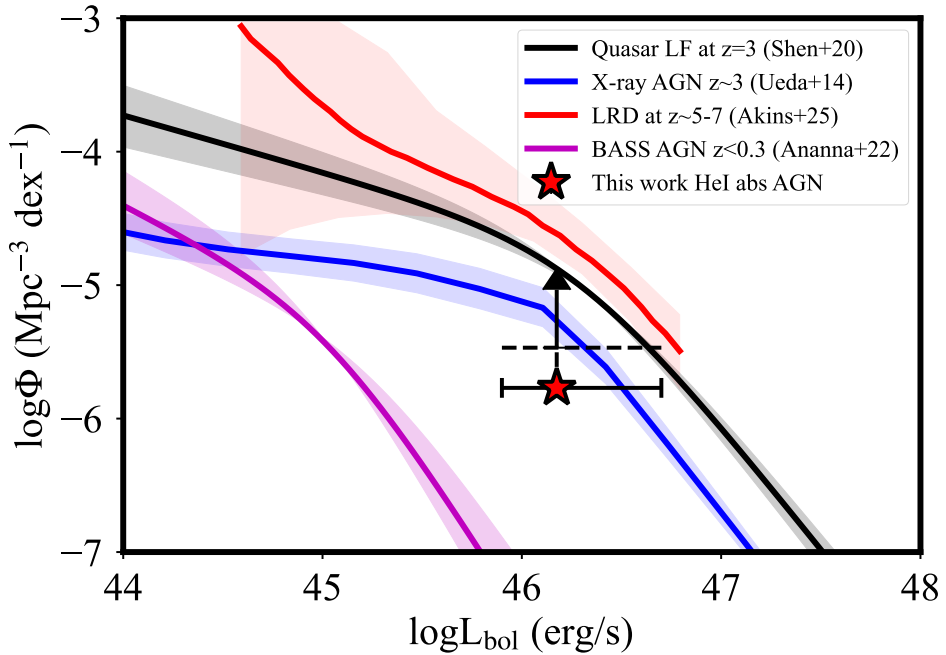


**Figure 6.** The luminosity function (LF) of different AGN populations. The red star is the LF of the  $\text{He I}\lambda 10830$  absorption AGNs reported in this work. The red star and the black dashed line indicates the lower limits, including two additional  $\text{He I}\lambda 10830$  absorption AGNs in the C3D fields with MIRI detections (one presented in Fu et al., submitted, and one with very weak HeI absorption,  $\log N_{\text{HeI}} < 12.0$ , which is not included in this work). The black line shows the quasar bolometric luminosity function (BLF) at  $z = 3$  from X. Shen et al. (2020). The green line represents the BLF of the X-ray AGN compilation in Y. Ueda et al. (2014). For comparison, we also include the BLF of LRDs at  $z \sim 5-7$  (red line; H. B. Akins et al. 2025) and the local X-ray sample from the BASS survey (purple line; T. T. Ananna et al. 2022).

contract at the University of Arizona. J-S.H acknowledges support from the Chinese Academy of Sciences (no. E52H540101). C.C. acknowledges NSFC grant No. 12173045, China Manned Space Program with grant no. CMS-CSST-2025-A07 and Chinese Academy of Sciences South America Center for Astronomy (CASSACA) Key Research Project no. E52H540301. J.-T.S. is supported by the Deutsche Forschungsgemeinschaft (DFG, German Research Foundation) - Project number 518006966.

This work is based on observations made with the NASA/ESA/CSA James Webb Space Telescope. The data were obtained from the Mikulski Archive for Space Telescopes at the Space Telescope Science Institute, which is operated by the Association of Universities for Research in Astronomy, Inc., under NASA contract NAS 5-03127 for JWST. These observations are associated

with programs #5893. Support for program #5893 was provided by NASA through a grant from the Space Telescope Science Institute, which is operated by the Association of Universities for Research in Astronomy, Inc., under NASA contract NAS 5-03127. We acknowledge the strong support provided by the program coordinator Alison Vick and instrument reviewers Brian Brooks and Jonathan Aguilar. Support for this work was provided by NASA through grant JWST-GO-01727 awarded by the Space Telescope Science Institute, which is operated by the Association of Universities for Research in Astronomy, Inc., under NASA contract NAS 5-26555.

*Facilities:* JWST, HST, Chandra, Keck:I (LRIS), Keck:II (DEIMOS), ALMA, Herschel, VLA

## REFERENCES

Aihara, H., Armstrong, R., Bickerton, S., et al. 2018, PASJ, 70, S8, doi: [10.1093/pasj/psx081](https://doi.org/10.1093/pasj/psx081)

Akins, H. B., Casey, C. M., Lambrides, E., et al. 2025, ApJ, 991, 37, doi: [10.3847/1538-4357/ade984](https://doi.org/10.3847/1538-4357/ade984)

Alexander, D. M., Bauer, F. E., Chapman, S. C., et al. 2005, ApJ, 632, 736, doi: [10.1086/444342](https://doi.org/10.1086/444342)

Álvarez-Márquez, J., Crespo Gómez, A., Colina, L., et al. 2023, A&A, 671, A105, doi: [10.1051/0004-6361/202245400](https://doi.org/10.1051/0004-6361/202245400)

Ananna, T. T., Weigel, A. K., Trakhtenbrot, B., et al. 2022, *ApJS*, 261, 9, doi: [10.3847/1538-4365/ac5b64](https://doi.org/10.3847/1538-4365/ac5b64)

Baldwin, J., Ferland, G., Korista, K., & Verner, D. 1995, *ApJL*, 455, L119, doi: [10.1086/309827](https://doi.org/10.1086/309827)

Bertin, E., Schefer, M., Apostolakos, N., et al. 2020, in *Astronomical Society of the Pacific Conference Series*, Vol. 527, *Astronomical Data Analysis Software and Systems XXIX*, ed. R. Pizzo, E. R. Deul, J. D. Mol, J. de Plaa, & H. Verkouter, 461

Boquien, M., Burgarella, D., Roehlly, Y., et al. 2019, *A&A*, 622, A103, doi: [10.1051/0004-6361/201834156](https://doi.org/10.1051/0004-6361/201834156)

Bruzual, G., & Charlot, S. 2003, *MNRAS*, 344, 1000, doi: [10.1046/j.1365-8711.2003.06897.x](https://doi.org/10.1046/j.1365-8711.2003.06897.x)

Bushouse, H., Eisenhamer, J., Dencheva, N., et al. 2025, JWST Calibration Pipeline, 1.19.1 Zenodo, doi: [10.5281/zenodo.6984365](https://doi.org/10.5281/zenodo.6984365)

Calzetti, D., Armus, L., Bohlin, R. C., et al. 2000, *ApJ*, 533, 682, doi: [10.1086/308692](https://doi.org/10.1086/308692)

Chabrier, G. 2003, *PASP*, 115, 763, doi: [10.1086/376392](https://doi.org/10.1086/376392)

Civano, F., Marchesi, S., Comastri, A., et al. 2016, *ApJ*, 819, 62, doi: [10.3847/0004-637X/819/1/62](https://doi.org/10.3847/0004-637X/819/1/62)

Ding, X., Silverman, J. D., & Onoue, M. 2022, *ApJL*, 939, L28, doi: [10.3847/2041-8213/ac9c02](https://doi.org/10.3847/2041-8213/ac9c02)

Ding, X., Silverman, J., Treu, T., et al. 2020, *ApJ*, 888, 37, doi: [10.3847/1538-4357/ab5b90](https://doi.org/10.3847/1538-4357/ab5b90)

Draine, B. T., Aniano, G., Krause, O., et al. 2014, *ApJ*, 780, 172, doi: [10.1088/0004-637X/780/2/172](https://doi.org/10.1088/0004-637X/780/2/172)

Duras, F., Bongiorno, A., Ricci, F., et al. 2020, *A&A*, 636, A73, doi: [10.1051/0004-6361/201936817](https://doi.org/10.1051/0004-6361/201936817)

Faber, S. M., & Gallagher, J. S. 1979, *ARA&A*, 17, 135, doi: [10.1146/annurev.aa.17.090179.001031](https://doi.org/10.1146/annurev.aa.17.090179.001031)

Fabian, A. C., Vasudevan, R. V., Mushotzky, R. F., Winter, L. M., & Reynolds, C. S. 2009, *MNRAS*, 394, L89, doi: [10.1111/j.1745-3933.2009.00617.x](https://doi.org/10.1111/j.1745-3933.2009.00617.x)

Fruscione, A., McDowell, J. C., Allen, G. E., et al. 2006, in *Society of Photo-Optical Instrumentation Engineers (SPIE) Conference Series*, Vol. 6270, *Observatory Operations: Strategies, Processes, and Systems*, ed. D. R. Silva & R. E. Doxsey, 62701V, doi: [10.1117/12.671760](https://doi.org/10.1117/12.671760)

Greene, J. E., Setton, D. J., Furtak, L. J., et al. 2025, arXiv e-prints, arXiv:2509.05434, doi: [10.48550/arXiv.2509.05434](https://doi.org/10.48550/arXiv.2509.05434)

Greene, T. P., Kelly, D. M., Stansberry, J., et al. 2017, *Journal of Astronomical Telescopes, Instruments, and Systems*, 3, 035001, doi: [10.1117/1.JATIS.3.3.035001](https://doi.org/10.1117/1.JATIS.3.3.035001)

Gunasekera, C. M., van Hoof, P. A. M., Dehghanian, M., et al. 2025, arXiv e-prints, arXiv:2508.01102, doi: [10.48550/arXiv.2508.01102](https://doi.org/10.48550/arXiv.2508.01102)

Harikane, Y., Zhang, Y., Nakajima, K., et al. 2023, *ApJ*, 959, 39, doi: [10.3847/1538-4357/ad029e](https://doi.org/10.3847/1538-4357/ad029e)

Hasinger, G., Capak, P., Salvato, M., et al. 2018, *ApJ*, 858, 77, doi: [10.3847/1538-4357/aabacf](https://doi.org/10.3847/1538-4357/aabacf)

Hickox, R. C., & Alexander, D. M. 2018, *ARA&A*, 56, 625, doi: [10.1146/annurev-astro-081817-051803](https://doi.org/10.1146/annurev-astro-081817-051803)

Hiremath, P., Rankine, A. L., Aird, J., et al. 2025, *MNRAS*, 542, 2105, doi: [10.1093/mnras/staf1352](https://doi.org/10.1093/mnras/staf1352)

Hönig, S. F., & Kishimoto, M. 2017, *ApJL*, 838, L20, doi: [10.3847/2041-8213/aa6838](https://doi.org/10.3847/2041-8213/aa6838)

Inayoshi, K., & Maiolino, R. 2025, *ApJL*, 980, L27, doi: [10.3847/2041-8213/adaebd](https://doi.org/10.3847/2041-8213/adaebd)

Ishibashi, W., Fabian, A. C., Ricci, C., & Celotti, A. 2018, *MNRAS*, 479, 3335, doi: [10.1093/mnras/sty1620](https://doi.org/10.1093/mnras/sty1620)

Ji, T., Zhou, H., Jiang, P., et al. 2015, *ApJ*, 800, 56, doi: [10.1088/0004-637X/800/1/56](https://doi.org/10.1088/0004-637X/800/1/56)

Jin, S., Daddi, E., Liu, D., et al. 2018, *ApJ*, 864, 56, doi: [10.3847/1538-4357/aad4af](https://doi.org/10.3847/1538-4357/aad4af)

Jones, B. L., Kocevski, D. D., Pacucci, F., et al. 2025, arXiv e-prints, arXiv:2510.07376, doi: [10.48550/arXiv.2510.07376](https://doi.org/10.48550/arXiv.2510.07376)

Juodžbalis, I., Ji, X., Maiolino, R., et al. 2024, *MNRAS*, 535, 853, doi: [10.1093/mnras/stae2367](https://doi.org/10.1093/mnras/stae2367)

Kocevski, D. D., Barro, G., McGrath, E. J., et al. 2023, *ApJL*, 946, L14, doi: [10.3847/2041-8213/acad00](https://doi.org/10.3847/2041-8213/acad00)

Kocevski, D. D., Finkelstein, S. L., Barro, G., et al. 2025, *ApJ*, 986, 126, doi: [10.3847/1538-4357/adbc7d](https://doi.org/10.3847/1538-4357/adbc7d)

Kokorev, V., Chisholm, J., Naidu, R. P., et al. 2025, arXiv e-prints, arXiv:2511.07515, <https://arxiv.org/abs/2511.07515>

Kormendy, J., & Ho, L. C. 2013, *ARA&A*, 51, 511, doi: [10.1146/annurev-astro-082708-101811](https://doi.org/10.1146/annurev-astro-082708-101811)

Koss, M., Trakhtenbrot, B., Ricci, C., et al. 2017, *ApJ*, 850, 74, doi: [10.3847/1538-4357/aa8ec9](https://doi.org/10.3847/1538-4357/aa8ec9)

Leauthaud, A., Massey, R., Kneib, J.-P., et al. 2007, *ApJS*, 172, 219, doi: [10.1086/516598](https://doi.org/10.1086/516598)

Lee, K.-G., Krolewski, A., White, M., et al. 2018, *ApJS*, 237, 31, doi: [10.3847/1538-4365/aace58](https://doi.org/10.3847/1538-4365/aace58)

Leighly, K. M., Terndrup, D. M., Baron, E., et al. 2014, *ApJ*, 788, 123, doi: [10.1088/0004-637X/788/2/123](https://doi.org/10.1088/0004-637X/788/2/123)

Li, J., Silverman, J. D., Ding, X., et al. 2021, *ApJ*, 918, 22, doi: [10.3847/1538-4357/ac06a8](https://doi.org/10.3847/1538-4357/ac06a8)

Li, R., Ho, L. C., & Chen, C.-H. 2025, arXiv e-prints, arXiv:2505.12867, doi: [10.48550/arXiv.2505.12867](https://doi.org/10.48550/arXiv.2505.12867)

Li, Z.-J., Dai, Y. S., Huang, J. S., Wuyts, S., & Cao, T.-W. 2024, *ApJ*, 963, 99, doi: [10.3847/1538-4357/ad1b54](https://doi.org/10.3847/1538-4357/ad1b54)

Lilly, S. J., Le Fèvre, O., Renzini, A., et al. 2007, *ApJS*, 172, 70, doi: [10.1086/516589](https://doi.org/10.1086/516589)

Lin, X., Wang, F., Fan, X., et al. 2024, *ApJ*, 974, 147, doi: [10.3847/1538-4357/ad6565](https://doi.org/10.3847/1538-4357/ad6565)

Lin, X., Fan, X., Cai, Z., et al. 2025, arXiv e-prints, arXiv:2507.10659, doi: [10.48550/arXiv.2507.10659](https://doi.org/10.48550/arXiv.2507.10659)

Liu, D., Lang, P., Magnelli, B., et al. 2019, *ApJS*, 244, 40, doi: [10.3847/1538-4365/ab42da](https://doi.org/10.3847/1538-4365/ab42da)

Liu, W.-J., Zhou, H., Ji, T., et al. 2015, *ApJS*, 217, 11, doi: [10.1088/0067-0049/217/1/11](https://doi.org/10.1088/0067-0049/217/1/11)

Loiacono, F., Gilli, R., Mignoli, M., et al. 2025, arXiv e-prints, arXiv:2506.12141, doi: [10.48550/arXiv.2506.12141](https://doi.org/10.48550/arXiv.2506.12141)

Lutz, D., Poglitsch, A., Altieri, B., et al. 2011, *A&A*, 532, A90, doi: [10.1051/0004-6361/201117107](https://doi.org/10.1051/0004-6361/201117107)

Lyu, J., Alberts, S., Rieke, G. H., et al. 2024, *ApJ*, 966, 229, doi: [10.3847/1538-4357/ad3643](https://doi.org/10.3847/1538-4357/ad3643)

Maiolino, R., Scholtz, J., Curtis-Lake, E., et al. 2024, *A&A*, 691, A145, doi: [10.1051/0004-6361/202347640](https://doi.org/10.1051/0004-6361/202347640)

Marchesi, S., Lanzuisi, G., Civano, F., et al. 2016, *ApJ*, 830, 100, doi: [10.3847/0004-637X/830/2/100](https://doi.org/10.3847/0004-637X/830/2/100)

Martínez-Ramírez, L. N., Calistro Rivera, G., Lusso, E., et al. 2024, *A&A*, 688, A46, doi: [10.1051/0004-6361/202449329](https://doi.org/10.1051/0004-6361/202449329)

Mathews, W. G., & Ferland, G. J. 1987, *ApJ*, 323, 456, doi: [10.1086/165843](https://doi.org/10.1086/165843)

Matthee, J., Naidu, R. P., Brammer, G., et al. 2024, *ApJ*, 963, 129, doi: [10.3847/1538-4357/ad2345](https://doi.org/10.3847/1538-4357/ad2345)

McCracken, H. J., Milvang-Jensen, B., Dunlop, J., et al. 2012, *A&A*, 544, A156, doi: [10.1051/0004-6361/201219507](https://doi.org/10.1051/0004-6361/201219507)

Naidu, R. P., Matthee, J., Kramarenko, I., et al. 2024, arXiv e-prints, arXiv:2410.01874, doi: [10.48550/arXiv.2410.01874](https://doi.org/10.48550/arXiv.2410.01874)

Oliver, S. J., Wang, L., Smith, A. J., et al. 2010, *A&A*, 518, L21, doi: [10.1051/0004-6361/201014697](https://doi.org/10.1051/0004-6361/201014697)

Ricci, C., Trakhtenbrot, B., Koss, M. J., et al. 2017a, *ApJS*, 233, 17, doi: [10.3847/1538-4365/aa96ad](https://doi.org/10.3847/1538-4365/aa96ad)

Ricci, C., Trakhtenbrot, B., Koss, M. J., et al. 2017b, *Nature*, 549, 488, doi: [10.1038/nature23906](https://doi.org/10.1038/nature23906)

Ricci, F., La Franca, F., Onori, F., & Bianchi, S. 2017, *A&A*, 598, A51, doi: [10.1051/0004-6361/201629380](https://doi.org/10.1051/0004-6361/201629380)

Ricci, F., Treister, E., Bauer, F. E., et al. 2022, *ApJS*, 261, 8, doi: [10.3847/1538-4365/ac5b67](https://doi.org/10.3847/1538-4365/ac5b67)

Sawicki, M., Arnouts, S., Huang, J., et al. 2019, *MNRAS*, 489, 5202, doi: [10.1093/mnras/stz2522](https://doi.org/10.1093/mnras/stz2522)

Schinnerer, E., Sargent, M. T., Bondi, M., et al. 2010, *ApJS*, 188, 384, doi: [10.1088/0067-0049/188/2/384](https://doi.org/10.1088/0067-0049/188/2/384)

Schreiber, C., Elbaz, D., Pannella, M., et al. 2018, *A&A*, 609, A30, doi: [10.1051/0004-6361/201731506](https://doi.org/10.1051/0004-6361/201731506)

Shankar, F., Dai, X., & Sivakoff, G. R. 2008, *ApJ*, 687, 859, doi: [10.1086/591488](https://doi.org/10.1086/591488)

Shen, X., Hopkins, P. F., Faucher-Giguère, C.-A., et al. 2020, *MNRAS*, 495, 3252, doi: [10.1093/mnras/staa1381](https://doi.org/10.1093/mnras/staa1381)

Shuntov, M., Akins, H. B., Paquereau, L., et al. 2025, arXiv e-prints, arXiv:2506.03243, doi: [10.48550/arXiv.2506.03243](https://doi.org/10.48550/arXiv.2506.03243)

Smolčić, V., Novak, M., Delvecchio, I., et al. 2017, *A&A*, 602, A6, doi: [10.1051/0004-6361/201730685](https://doi.org/10.1051/0004-6361/201730685)

Stalevski, M., Fritz, J., Baes, M., Nakos, T., & Popović, L. Č. 2012, *MNRAS*, 420, 2756, doi: [10.1111/j.1365-2966.2011.19775.x](https://doi.org/10.1111/j.1365-2966.2011.19775.x)

Stalevski, M., Ricci, C., Ueda, Y., et al. 2016, *MNRAS*, 458, 2288, doi: [10.1093/mnras/stw444](https://doi.org/10.1093/mnras/stw444)

Steinhardt, C. L., Speagle, J. S., Capak, P., et al. 2014, *ApJL*, 791, L25, doi: [10.1088/2041-8205/791/2/L25](https://doi.org/10.1088/2041-8205/791/2/L25)

Sun, F., Egami, E., Pirzkal, N., et al. 2023, *ApJ*, 953, 53, doi: [10.3847/1538-4357/acd53c](https://doi.org/10.3847/1538-4357/acd53c)

Temple, M. J., Hewett, P. C., & Banerji, M. 2021, *MNRAS*, 508, 737, doi: [10.1093/mnras/stab2586](https://doi.org/10.1093/mnras/stab2586)

Trakhtenbrot, B., Urry, C. M., Civano, F., et al. 2015, *Science*, 349, 168, doi: [10.1126/science.aaa4506](https://doi.org/10.1126/science.aaa4506)

Treister, E., & Urry, C. M. 2006, *ApJL*, 652, L79, doi: [10.1086/510237](https://doi.org/10.1086/510237)

Ueda, Y., Akiyama, M., Hasinger, G., Miyaji, T., & Watson, M. G. 2014, *ApJ*, 786, 104, doi: [10.1088/0004-637X/786/2/104](https://doi.org/10.1088/0004-637X/786/2/104)

Vivek, M., & Wylezalek, D. 2025, *A&A*, 695, L22, doi: [10.1051/0004-6361/202453352](https://doi.org/10.1051/0004-6361/202453352)

Wang, B., Ishikawa, Y., Hennawi, J. F., et al. 2025a, *MNRAS*, doi: [10.1093/mnras/staf1730](https://doi.org/10.1093/mnras/staf1730)

Wang, B., de Graaff, A., Davies, R. L., et al. 2025b, *ApJ*, 984, 121, doi: [10.3847/1538-4357/acd1ca](https://doi.org/10.3847/1538-4357/acd1ca)

Weaver, J. R., Kauffmann, O. B., Ilbert, O., et al. 2022, *ApJS*, 258, 11, doi: [10.3847/1538-4365/ac3078](https://doi.org/10.3847/1538-4365/ac3078)

Whitaker, K. E., van Dokkum, P. G., Brammer, G., & Franx, M. 2012, *ApJL*, 754, L29, doi: [10.1088/2041-8205/754/2/L29](https://doi.org/10.1088/2041-8205/754/2/L29)

Wu, Q., Shen, Y., Guo, H., et al. 2025, *ApJ*, 980, 134, doi: [10.3847/1538-4357/ada386](https://doi.org/10.3847/1538-4357/ada386)

Zhang, S., Zhou, H., Shi, X., et al. 2015, *ApJ*, 815, 113, doi: [10.1088/0004-637X/815/2/113](https://doi.org/10.1088/0004-637X/815/2/113)

Zhuang, M.-Y., & Ho, L. C. 2023, *Nature Astronomy*, 7, 1376, doi: [10.1038/s41550-023-02051-4](https://doi.org/10.1038/s41550-023-02051-4)

Zhuang, M.-Y., Li, J., & Shen, Y. 2024, *ApJ*, 962, 93, doi: [10.3847/1538-4357/ad1517](https://doi.org/10.3847/1538-4357/ad1517)

Zhuang, M.-Y., & Shen, Y. 2024, *ApJ*, 962, 139, doi: [10.3847/1538-4357/ad1183](https://doi.org/10.3847/1538-4357/ad1183)

## APPENDIX

## A. FIGURES

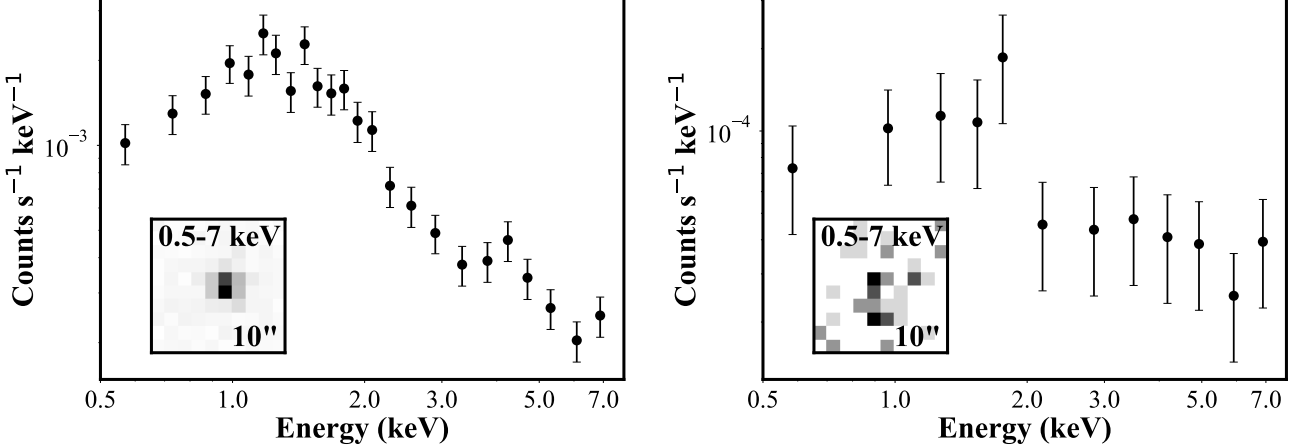


**Figure A1.** 0.5-7 keV X-ray imaging and spectroscopy for `cid_414` (left) and `cid_947` (right). The X-ray observations are from Chandra COSMOS Legacy survey (F. Civano et al. 2016). We use CIAO 4.17 (A. Fruscione et al. 2006) to reduce the Chandra data with a 4.12.2 version of calibration database (CALDB). The data are reprocessed by the script `chandra_repro`. The background flares are removed by the command `deflare`. The X-ray imaging is generated from a merged event list by `merge_obs`. We extract the spectrum in the region enclosing 90% PSF at 1 keV for each observation with `specextract` script. The spectra are then combined and grouped to have at least 10 counts in each energy bin.

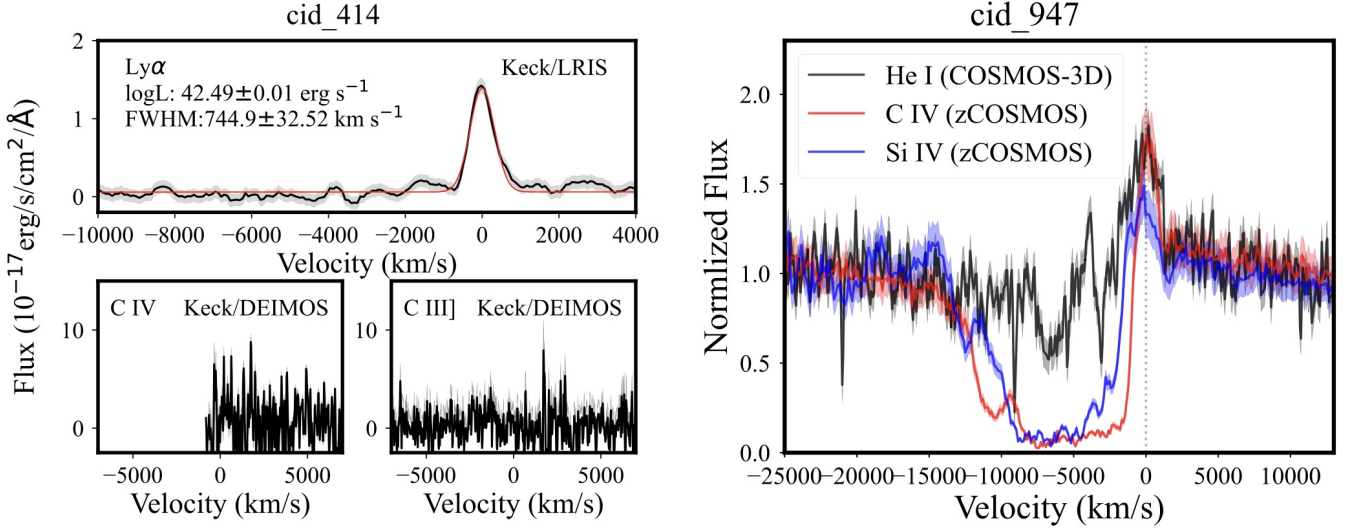


**Figure A2.** Archival Keck spectra for `cid_414` (left) and `cid_947` (right). A clear Ly $\alpha$  emission line is detected for `cid_414` in the CLAMATO survey (K.-G. Lee et al. 2018), while no C IV or C III] emission is seen in the Keck/DEIMOS spectrum with an exposure time of 1800 s. In the right panel, we show the velocity profiles of the broad-absorption AGN `cid_947`, including He I $\lambda 10830$ , C IV, and Si IV.

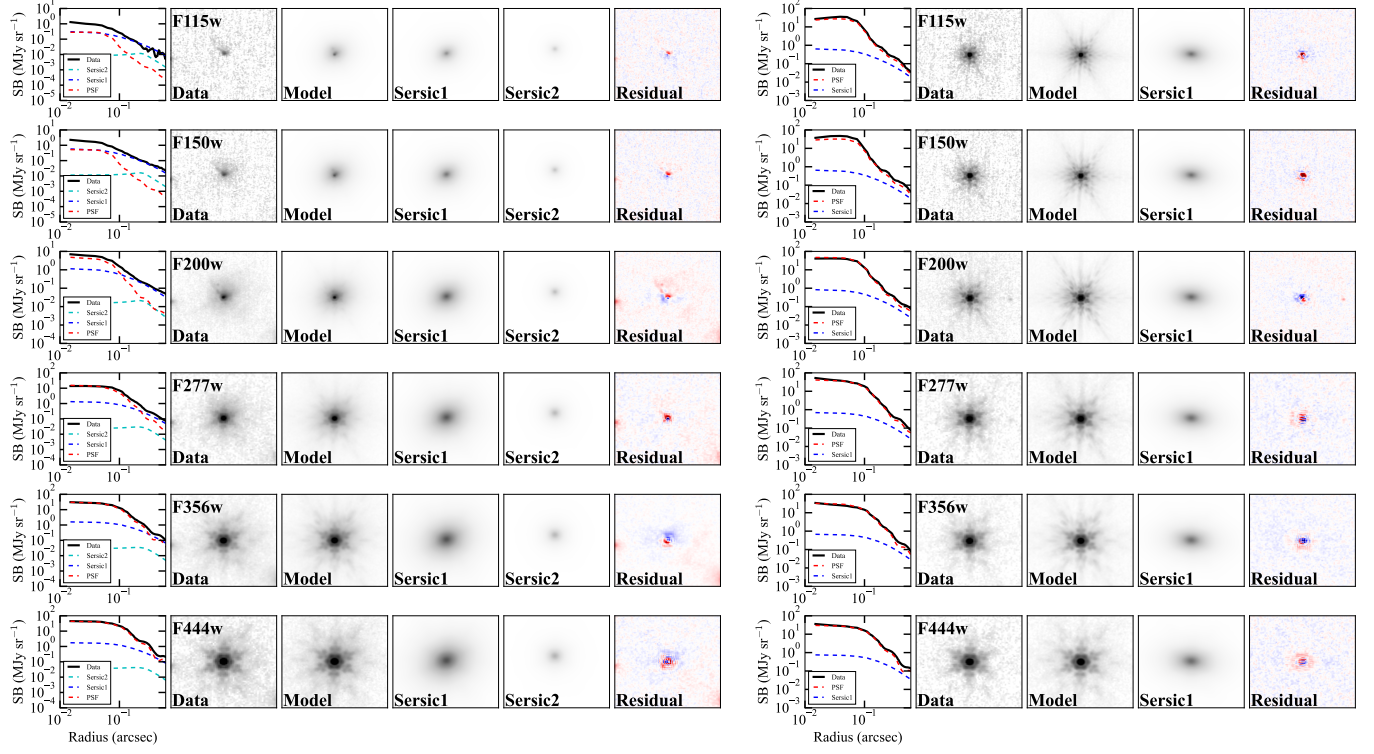


**Figure A3.** Multiband JWST imaging decomposition for `cid_414` (left) and `cid_947` (right) using `GALFITS` (R. Li et al. 2025). The 1D surface-brightness (SB) profiles as a function of radius are shown in the first panel of each row. The data and model images are displayed using the same logarithmic stretch, while the residual (data-model divided by the sigma image) is shown linearly over a range of  $-10$  to  $10$ . We model `cid_414` with two Sérsic components. In the F115W and F150W bands, the SB of the second Sérsic component exceeds that of the first beyond  $\sim 0.^{\prime\prime}1$ .